Mixed-mode fracture in a soft elastomer

Yinan Lu¹, Yuan Qi¹, Michely Tenardi¹, Rong Long^{1*}

¹Department of Mechanical Engineering, University of Colorado Boulder, Boulder CO 80309,

USA

*Corresponding author: rong.long@colorado.edu

Abstract

We present an experimental study on mixed-mode crack propagation in thin sheet specimens of a soft silicone elastomer. To introduce mixed-mode loading, we adopted the widely applied pure shear fracture testing geometry, but oriented the initial crack at an inclined angle relative to the direction perpendicular to the external tensile loading. Because of the inclined angle, locally the crack tip was subjected to both tensile and shear loading even though the global loading was tensile, thus resulting in a mixed Mode-I and Mode-II condition for the crack. Altering the inclined angle led to different degrees of mode-mixity and hence different crack propagation trajectories. Using a particle tracking method, we were able to measure the nonlinear deformation fields throughout the entire course of crack propagation. Based on the measured deformation fields, we used J-integral to calculate the energy release rate during crack propagation and found that the results were insensitive to the tangent direction of the crack trajectory, suggesting that the fracture toughness was approximately mode independent. Moreover, the tangent direction of the crack trajectory, when plotted in the reference configuration, was observed to be perpendicular to the direction of maximum principal stretch. The experimental results pave the way for establishing quasi-static mixed-mode fracture criteria for soft silicone elastomer, which has not yet been well understood in the literature.

Keywords: mixed-mode, crack propagation, soft material, fracture toughness, particle tracking, large deformation.

1. Introduction

Soft polymeric materials with high deformability have been widely applied in many technological applications. Examples include sealant [1], pressure sensitive adhesives [2], soft robotics [3], biomedical devices [4], and stretchable electronics [5]. In these applications, the underlying soft materials are required to undergo large deformation and yet resist fracture. Fracture refers to the deformation and propagation of originally sharp cracks and is a major failure mode in soft materials. Experimental characterization of crack propagation in soft materials was first carried out in rubber [6] and more recently extended to hydrogels and elastomers [7–10]. Most fracture testing configurations for soft materials have been focused on the Mode-I condition where the crack opens symmetrically under a tensile loading perpendicular to it. Specifically, the pure shear test [6], simple extension test [6] and single edge notch test [11], which represent the most frequently adopted fracture test configurations for rubber, elastomers and hydrogels, can all be categorized as Mode-I. There are a few exceptions such as the tearing test [12] where the crack is mainly subjected to an out-of-plane shear loading (i.e., Mode-III) and the lap-shear fracture test [13] or bilayer stretch test [14] where the crack is mainly subjected to an in-plane shear loading (i.e., Mode-II). Although the latter two tests are designed for characterizing adhesive fracture between two dissimilar soft materials, in principle they can also be used to study cohesive fracture in a single soft material.

A unique challenge with soft material fracture is the nonlinearity associated with large deformation of the crack. In linear elastic fracture mechanics (LEFM), the crack tip deformation field can always be decomposed into the superposition of three basic fracture modes. However, such mode decomposition is no longer valid in soft materials because the superposition principle breaks down under large deformation. For example, theoretical analyses suggest that pure Mode-II solution, which is anti-symmetric about the crack, does not exist under the framework of nonlinear elasticity [15–17]. Note that these analyses were based on the fully nonlinear governing equations of hyperelasticity, which require the assumption of certain hyperelastic models. To draw general conclusions for isotropic homogeneous solids, Knowles [18] considered a "small-scale nonlinear" problem where the crack was subjected to pure Mode-II loading far away from the crack tip, and found that nonlinear effects would lead to crack opening or interpenetration (i.e., Mode-I deformation) near the crack tip. This conclusion, implying the non-existence of pure Mode-II solution under nonlinear elasticity, was also derived by Harpaz and Bouchbinder [19]

using the weakly nonlinear elastic theory (i.e., second-order nonlinearity in addition to the first-order linear elasticity), which covers both the quasi-static and dynamic regimes. Therefore, under large deformation, a two-dimensional (2D) crack (i.e., plane strain or plane stress) can only be subjected to pure Mode-I or mixed-mode conditions.

In practice, mixed-mode (Mode-I and II) crack propagation is particularly relevant when interfaces between dissimilar materials are present. For example, Wang et al. [20] demonstrated that composites combining a soft elastic matrix and stiff elastic inclusions exhibit high toughness, low hysteresis and high fatigue threshold [21]. The key underlying mechanism is that when a crack propagating in the soft matrix approaches a stiff inclusion, the crack is deflected away from its original propagating direction, presumably due to the mixed-mode condition near the inclusion interface. Similarly, by engineering z-shaped soft domains in a stiff polymer, Cox et al. [22] achieved crack guiding along tortuous paths under global tensile loading, which also relied on the mixed-mode condition near the interface. Despite the theoretical significance and practical relevance, experimental studies on mixed-mode fracture of soft materials has been very limited. Unlike adhesive fracture of soft materials where one can control mode-mixity (e.g., by changing the peel angle in a peel test [23]), it can be challenging to experimentally characterize mixedmode cohesive fracture in soft materials due to large deformation near the crack tip. Few studies have been dedicated to this problem. In Sun et al. [24], tearing test (i.e., out-of-plane shear loading) was applied to a tough hydrogel, resulting in a fracture toughness comparable to that measured from the Mode-I pure shear fracture test. Ronsin et al. [25] found that a crack in gelatin gels under mixed Mode-I and Mode-III condition is subjected to a échelon instability. To the best of our knowledge, there has been no experimental studies for crack propagation in soft materials with controllable mode-mixity between tensile (Mode-I) and in-plane shear (Mode-II) loading.

In this paper, we present an experimental approach where mixed-mode condition is introduced by orienting the initial crack in the pure shear test geometry at an inclined angle $\theta \ge 0$ to the horizontal direction (Fig.1a). Stress transformation implies that the inclined crack will be subjected to a combination of tensile and shear loadings with respect to a local coordinate system $x'_1-x'_2$ aligned with the crack. Our goal is to understand the critical conditions governing the mixed-mode crack propagation, which consist of two components: fracture toughness and crack propagation direction. First, the fracture toughness Γ , defined as the energy required to advance

a crack by a unit area, characterizes a material's capability to resist crack growth. For quasi-static crack propagation in an elastic solid, linear or nonlinear, equilibrium dictates that Γ is equal to the energy release rate G representing the energetic driving force supplied by external loading [26]. In conventional pure shear geometry (i.e., $\theta = 0$), G can be readily calculated using the global stretch $\lambda = 1 + \Delta/H$, where Δ is the applied displacement and H is the sample height [27]. However, when $\theta > 0$, the equation relating G and the global stretch λ is no longer valid due to the loss of symmetry and translational invariance. Alternatively, for elastic solids, G can also be evaluated by a path-independent J-integral that encloses the crack tip [28], but this would require the deformation and stress fields around the crack. Second, under mixed-mode loading, the direction of crack propagation is not known a-priori. In LEFM, multiple criteria have been developed to predict the direction of mixed-mode crack propagation [26]. Little is known about what kind of criterion should be imposed for mixed-mode crack propagation with large deformation. Evaluation of the J-integral and assessment of the criterion for crack propagation direction both require knowledge of the deformation and stress fields in the specimen during crack propagation. Using a soft silicone elastomer as a model system, we demonstrate full-field measurement of the in-plane displacement, deformation gradient and stress components by tracking randomly distributed tracer particles on the sample [29]. The measured deformation fields also allow us to map the crack tip identified in the deformed configuration back to the reference configuration, thus enabling the definition of true crack extension length and speed in the reference configuration. These measurements make quantitative characterization of mixed-mode crack propagation possible. The experimental method is summarized in Section 2. In Section 3, we first describe experimental observations on crack propagation and the associated deformation and stress fields, followed by a quantitative discussion on the mixed-mode fracture toughness Γ and the criterion for crack propagation direction. Conclusions are made in Section 4.

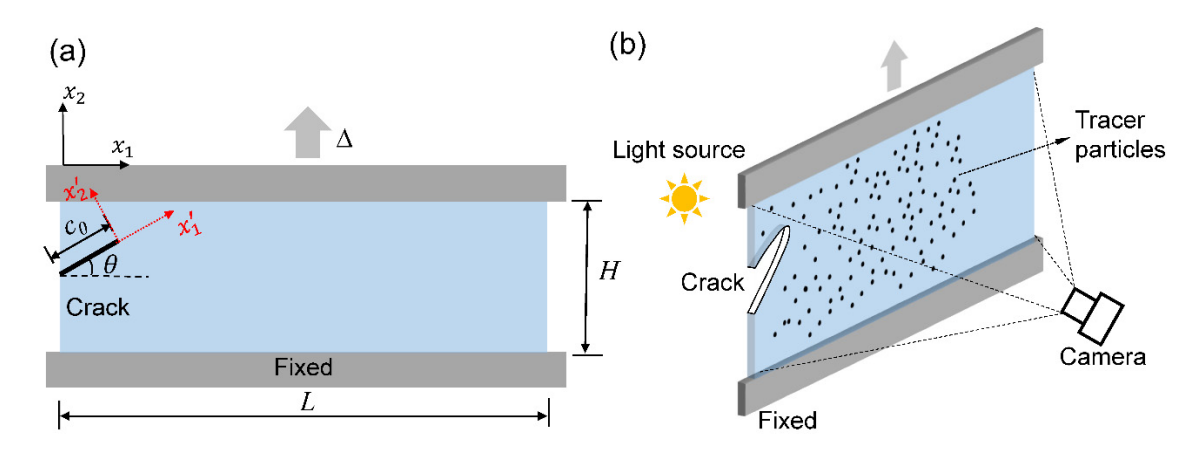


Figure 1 Experimental configuration of the mixed-mode fracture test. (a) Geometry of the pure-shear fracture test with an inclined initial crack. (b) A schematic showing the tracer particles deposited on the sample surface and the imaging setup.

2. Materials and Method

Material samples were made of a stretchable silicone elastomer, Ecoflex 00-30 (Smooth-On Inc., Macungie, PA, USA). This elastomer, recently used in our study of Mode-I fracture [29], was selected in this work for two reasons. First, its low modulus and moderate fracture toughness result in severe blunting of the crack tip during crack propagation [29], thereby allowing us to include the effects of large deformation. Second, this elastomer behaves as a hyperelastic solid with negligible hysteresis except in the vicinity of the crack tip [29], which justifies the application of J-integral. The samples were prepared as follows. We first mixed the Part A and Part B precursors of Ecoflex 00-30 in a 1:1 ratio, and deposited the mixture into a 100 mm × 100 mm × 1.5 mm acrylic mold. After degassing for 20 minutes, the precursor mixture was heated and cured at 80 °C for 30 minutes. After cooling down and left at room temperature for one day, the thin-sheet sample was removed from the mold and a tilted crack was cut at the edge of the sample by a razor blade (see Fig.1a). Prior to each experiment, we randomly brushed black glass beads with a diameter of 150 μm ~ 180 μm (Cospheric, Santa Barbara, CA, USA) on one face of the sample. These black beads remained adhered to the sample surface during the entire course of an experiment, and thus were used as tracer particles for measuring the displacement and strain fields as the tilted crack deforms and propagates.

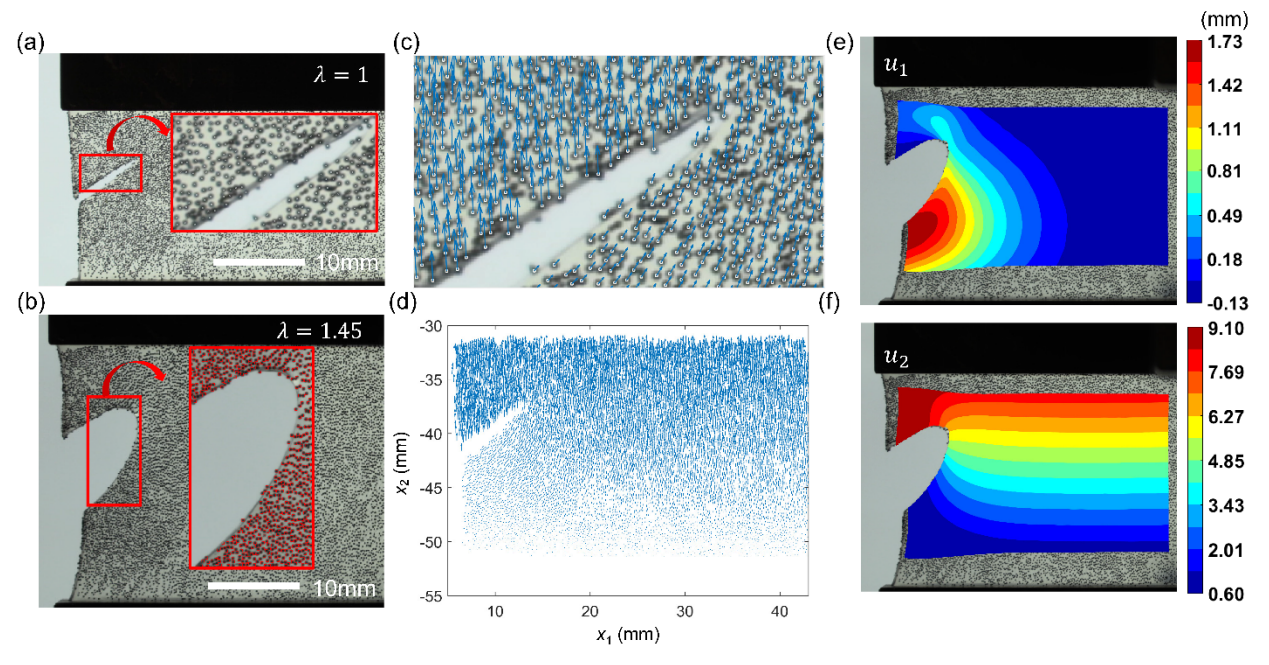


Figure 2 Particle tracking method for measuring displacement field. (a-b) Images of the fracture sample and tracer particles (a) before deformation (i.e., global stretch $\lambda = 1+\Delta/H = 1$) and (b) in the deformed configuration with ($\lambda = 1.45$). The insets show zoomed-in views of the crack tip region. (c) Displacement vectors of tracer particles near the crack tip tracked between two time frames of $\lambda = 1$ and 1.06. (d) Quiver plot showing the displacements of ~12,000 tracer particles tracked between $\lambda = 1$ and 1.45. (e-f) Color contours of displacement components u_1 (horizontal) and u_2 (vertical) interpolated from tracer particle displacements.

We conducted fracture experiments following the pure shear test geometry except that the initial crack was tilted at an inclined angle (Fig.1a). The thin-sheet elastomer sample was clamped by two sets of rigid plates, leaving a long strip area for fracture testing with dimensions of width L=100 mm, height H=22 mm and thickness t=1.5 mm. The initial crack, starting at the middle of the left edge of the sample, had a length of $c_0=10$ mm and an initial tilt angle $\theta (\geq 0)$. Five different initial tilt angles were tested: $\theta=0^{\circ}$, 15° , 30° , 45° , and 60° . The sample was mounted on a mechanical testing machine (Instron 5965). A displacement Δ was applied at the top edge with a fixed global strain rate of $\dot{\Delta}/H=0.01~{\rm s}^{-1}$, while the bottom edge remained fixed. Meanwhile, the sample deformation and crack propagation were imaged by a 4K high-speed camera (Canon XC10) at 30 frames per second with a typical resolution of 25 μ m per pixel (resolution: 3840 \times 2160). To enhance the contrast between the tracer particles and the background, we used a white light source on the opposite side of the camera to illuminate the sample (Fig.1b).

Images of the tracer particles allowed us to measure the in-plane displacement and strain fields in the sample using the particle tracking method described in our recent work [29]. This method, consisting of the following four steps, has been demonstrated to capture the large deformation around a Mode-I crack in the Ecoflex 00-30 elastomer with high resolution and accuracy.

- First, a video processing software (Canon XF Utility) was employed to extract individual time
 frame from the video. To increase the efficiency of image processing, we extracted one frame
 per 3s before crack propagation started. After the crack started to propagate, we increased the
 frequency of extraction to 1 ~ 30 frames per second depending on the speed of crack
 propagation.
- Second, since each tracer particle appeared as a black circle, we used the built-in function *imfindcircle()* in MATLAB (Mathworks, Natick, MA, USA) to determine the in-plane coordinates of centroid for each tracer particle at each time frame. Examples of the identified centroids of tracer particles at two different time frames of an experiment are shown in Fig.2a and 2b, respectively.
- Third, we applied the Feature-Vector-Relaxation Method (FVRM) [30] to track the tracer particles in two consecutive time frames. The underlying principle of FVRM is to use the relative positions of neighboring particles around a tracer particle as a geometrical signature for tracking. A representative tracking result is shown in Fig.2c. By linking the tracked pairs from the first to the last time frame, we determined the trajectories of the tracer particles during the experiment, resulting in a set of discrete displacement data at any time frame (see Fig.2d for example).
- Fourth, given that the tracer particles are randomly distributed, we adopted the Moving Least Square (MLS) interpolation method [31] to calculate a continuous displacement field at each time frame from the discrete displacement data at the tracer particles (see Fig.2e and 2f for example). The MLS interpolation method, originally developed for the mesh-free methods [32] in computational mechanics, is particularly suitable for our tracer particles, since it does not require a certain geometrical structure of the data points. Once a continuous displacement field was determined, spatial gradients of the displacement field were used to compute the strain fields.

Evaluation of stress fields based on the measured strain fields requires a constitutive model for the underlying elastomer. Following our recent work [29], we modeled the Ecoflex 00-30 elastomer as an incompressible hyperelastic solid. In particular, we adopted the generalized neo-Hookean model (GNH) to derive the stress-strain relation, and performed uniaxial tensile tests to calibrate the material parameters. Considering the potential sample-to-sample variations in mechanical properties, for each fracture sample we cut two strips (10 mm \times 35 mm \times 1.5 mm) from unused part of the sample to conduct uniaxial tensile tests (nominal strain rate = 10^{-2} s⁻¹).

3. Results and Discussions

3.1 Crack propagation

We first examine the crack propagation trajectory as a manifestation of the mixed-mode condition imposed on the tilted crack. Figure 3a shows the global force-displacement response measured for a crack with initial tilt angle $\theta = 0^{\circ}$, 30° , or 60° . Images of the sample corresponding to different points on the global force-displacement curve are shown in Fig.3b. We observed that the tilted crack first opened asymmetrically about the initial crack direction (see Frame 2-3 for the case of $\theta = 30^{\circ}$ and 60° in Fig.3b) and then took a curved trajectory after it started to propagate (see Frame 4 in for the case of $\theta = 30^{\circ}$ and 60° in Fig.3b). During crack propagation, the crack underwent a large opening displacement, causing the crack tip to become blunted. The postmortem image (Frame 5 in Fig.3b) allowed us to extract the trajectory of crack tip by examining the fractured edge of the sample. The crack trajectory was found to depend on the initial crack angle, as demonstrated by the comparison between the two cases of $\theta = 30^{\circ}$ and 60° in Fig.3c. Both the asymmetric opening and curved trajectory imply that the tilted crack was subjected to a mixed-mode loading condition. The case of $\theta = 0^{\circ}$ was used as a control, where the initial crack was subjected to pure Mode-I loading. As expected, in this case the crack took a straight, horizontal trajectory after it started to propagate (see Fig.3c). Interestingly, regardless of the initial tilt angle, the crack trajectory always converged to the horizontal direction, i.e., perpendicular to the global tensile loading.

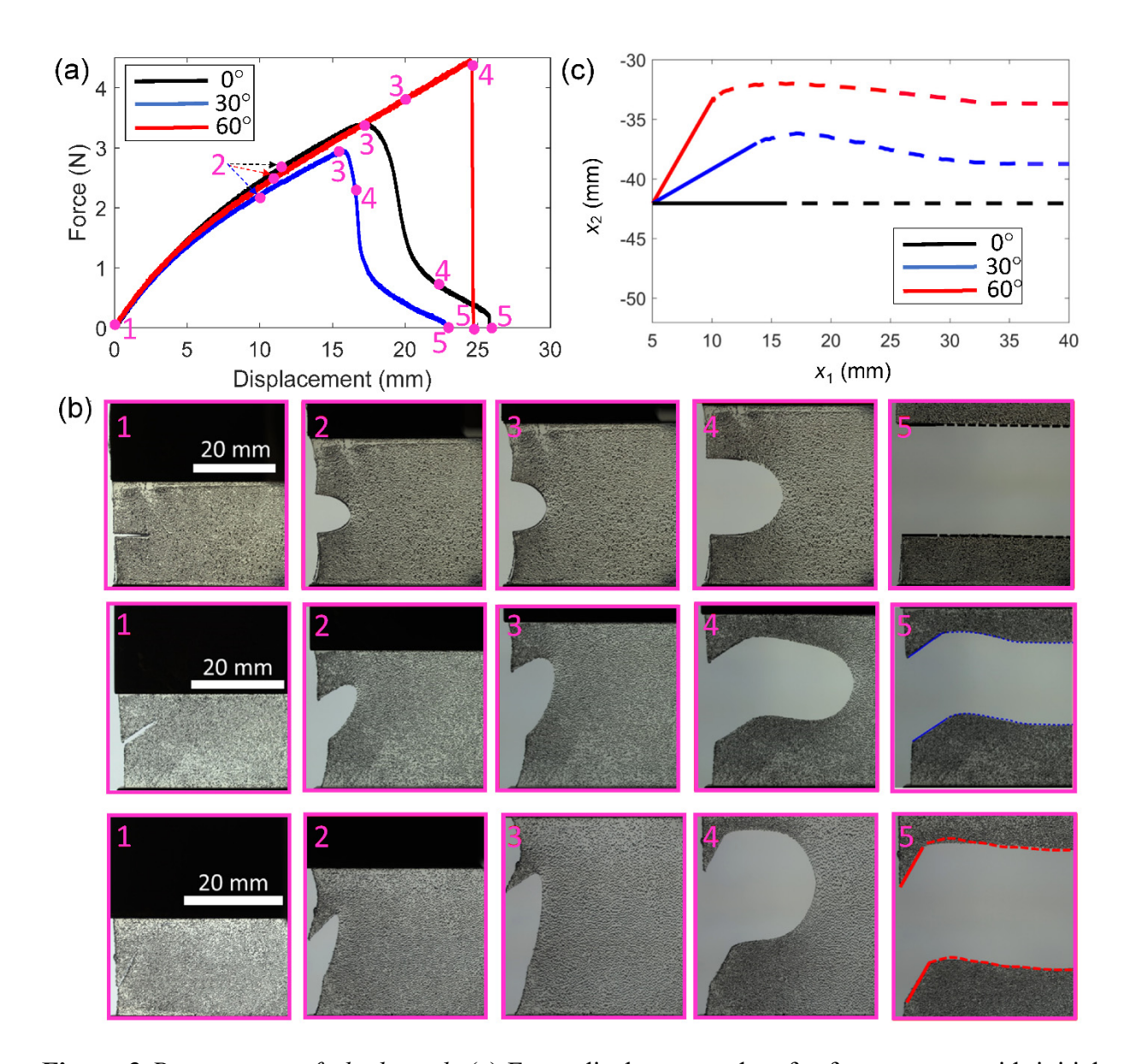


Figure 3 Propagation of tilted crack. (a) Force-displacement data for fracture tests with initial tilt angle $\theta = 0^{\circ}$, 30° or 60° . (b) Images showing crack deformation and propagation at five different time frames in cases with initial tilt angle $\theta = 0^{\circ}$ (top row), 30° (middle row), or 60° (bottom row). The curves superimposed to Frame 5 represent the crack tip trajectories obtained from the edges of the fractured samples. (c) Crack tip trajectory extracted from the post-mortem images of fractured sample for the three cases with $\theta = 0^{\circ}$, 30° , and 60° (solid lines: initial crack; dashed lines: crack propagation trajectory).

An important phenomenon we observed is that the crack propagation accelerated significantly after the peak global force was reached (e.g., Frame 4 to 5 in Fig.3a-3b). Measurement of the crack propagation speed would require us to identify the length of crack extension at each time frame. Since large deformation alone can displace the crack tip, the crack extension length should

be measured in the reference configuration to decouple crack propagation from large deformation. Although the crack trajectory extracted from the post-mortem image (Fig.3c) is with respect to the reference configuration, the corresponding location of the crack tip at a given time frame on the trajectory is still unknown. To address this problem, we followed an iterative process developed in our previous work [29] which leveraged the displacement field obtained from particle tracking (see Figs.2e-2f for example). The displacement field, essentially a forward mapping from the reference configuration to the deformation configuration at any time frame, enabled us to map the crack tip in the deformation configuration back to the reference configuration. Briefly, we first identified the crack tip position in the deformed configuration of each frame (e.g., see red dots in the insets of Fig.4a) which will be referred to as the target. Next, an initial guess of the crack tip position in the reference configuration was made, which was then fed into the MLS interpolation program to determine its displacement and hence the projected position in the deformation configuration. If the distance between the projected position and the target was smaller than a prescribed threshold, the guessed position was taken as the crack tip position in reference configuration. Otherwise, a new guess was made to bring its projected position in the deformed configuration closer to the target. This process was repeated until the projected crack tip position converged to the target in the deformed configuration. Using this method, we were able to determine the reference crack tip position for each time frame. The crack propagation trajectory emerged when these reference crack tip positions were put together, which agreed well with that extracted from post-mortem image of the sample (Fig.4a).

Because of the curved crack trajectory, we define the reference crack extension length as the arc length measured from the initial crack tip (see Δc in Fig.4a). The iterative process described above allowed us to determine Δc for each time frame, as shown in Fig.4b using the case with initial tilt angle $\theta = 30^{\circ}$ as an example. Note that $\lambda - 1 \equiv \Delta/H$ is proportional to time since the global displacement Δ was applied with a constant rate. It can be seen that Δc first remained zero and then rapidly increased after crack propagation started. We define the reference crack speed V as the time derivative of Δc :

$$V = \frac{d\left(\Delta c\right)}{dt} \ . \tag{1}$$

For a given frame, V was evaluated by the backward difference scheme using the current and the immediate preceding frames. The data of V versus the global stretch λ obtained for the case with $\theta = 30^{\circ}$ are shown in Fig.4c. Although in principle V should be zero before the crack started to propagate, we found that V was scattered but remained below about 10^{-2} mm/s for small λ , which is attributed to the uncertainty of mapping the crack tip in the deformed configuration back to the reference configuration. It is difficult to theoretically estimate the noise level in the reference crack speed V due to the large deformation involved in the mapping process, but the data in Fig.4c suggest that it is approximately 10^{-2} mm/s or below.

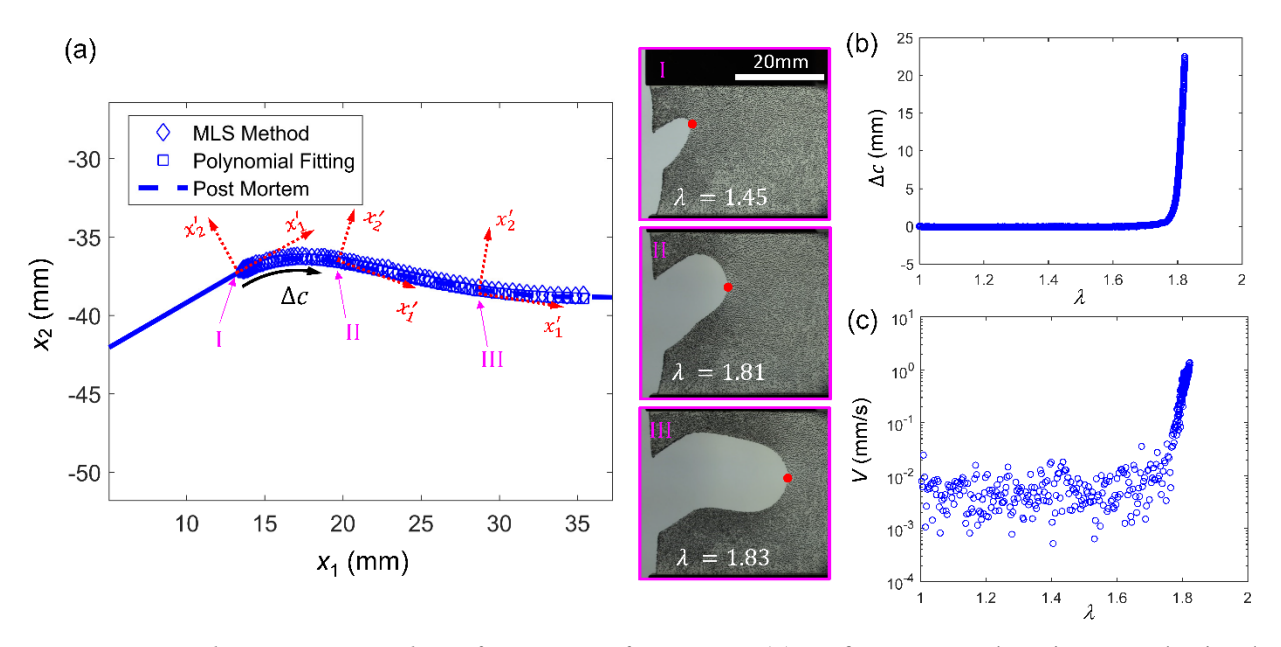


Figure 4 *Crack trajectory in the reference configuration*. (a) Reference crack trajectory obtained from MLS mapping (diamond symbols) and post-mortem examination (dashed line). The initial crack is represented by a solid line. The insets show the deformed configurations at three different frames: I, II and III, where the red dots represent the crack tip locations. A 7th-order polynomial fitting (square symbols) was used to smoothen the crack trajectory data, based on which the crack propagation direction (i.e., tangent of the crack trajectory) is found, as illustrated by the local x'_1 -axis. (b) Reference crack extension length Δc versus global stretch λ . (c) Reference crack speed V versus global stretch λ . All data are for the case with initial tilt angle $\theta = 30^{\circ}$.

The direction of crack propagation is also desired for understanding the mixed-mode fracture. To represent the crack propagation direction, we built a local coordinate system x'_1 - x'_2 at the crack tip that was aligned with the tangent direction of the crack trajectory in the reference configuration (Fig.4a). However, the MLS mapping to locate crack tip in the reference configuration inevitably resulted in noises in the crack trajectory data, making it impractical to directly extract the tangent

direction from the crack trajectory. Therefore, we applied a smoothening step by using a 7th-order polynomial function $x_2 = g(x_1)$ to fit the crack trajectory data (see Fig.4a). The choice of this fitting function was purely empirical: we found that lower order polynomial functions were not sufficient to fit the crack trajectories and the 7th-order polynomial was needed to accurately capture the tangent direction of the crack trajectory. For each crack trajectory, we have compared the fitted function and the experimental data to ensure there was no overfitting. After the smoothening step, we were able to reliably evaluate the crack propagation direction (i.e., the x'_1 -axis) for any frame by calculating the derivative dx_2/dx_1 based on the fitted polynomial function.

3.2 Deformation and stress fields during crack propagation

This main goal of this work is to quantitatively characterize the mixed-mode fracture behaviors of soft elastomer by measuring the deformation and stress fields associated with crack propagation. Such data would allow us to evaluate the energy release rate G through J-integral and to understand the crack propagation direction. Because of the large deformation involved in our experiments, we adopted the theory of finite strain kinematics and used the deformation gradient tensor \mathbf{F} as the metric for deformation. The in-plane components of \mathbf{F} are given by

$$F_{\alpha\beta} = \delta_{\alpha\beta} + \frac{\partial u_{\alpha}}{\partial x_{\beta}} \quad (\alpha, \beta = 1, 2), \tag{2}$$

where $\delta_{\alpha\beta}$ is the Kronecker delta (i.e., equal to 1 if $\alpha = \beta$ and 0 otherwise), x_{β} is the coordinate of a material point in the reference configuration, and u_{α} is the in-plane displacement component of this material point. Because of the thin-sheet shape of our samples, we assume plane stress condition which implies $F_{\alpha\beta} = F_{3\alpha} = 0$ ($\alpha = 1, 2$). The incompressibility constraint dictates that the out-of-plane stretch is

$$F_{33} \equiv \lambda_3 = \frac{1}{F_{11}F_{22} - F_{12}F_{21}}. (3)$$

To interpolate the discrete displacement data at tracer particles into a continuous field, we applied the MLS method which required polynomial basis and a weight function [31]. Similar to our recent work [29], we adopted the linear polynomial basis and an exponential weight function with a cut-off radius $r_c = 1$ mm. After interpolation, we computed the gradients of the continuous

displacement field to obtain the fields of $F_{\alpha\beta}$ at each time frame. Examples of the measured deformation fields, plotted in the reference configuration, are shown in Fig.5 under four different global stretches λ for the case with initial tilt angle $\theta = 30^{\circ}$. The highly amplified deformation at the crack tip is evident from the fields plotted in Fig.5. Moreover, we observed that the deformation fields were asymmetric about the initial tilted crack (e.g., see F_{11} at $\lambda = 1.45$ and 1.75). As the crack propagation proceeded, the crack trajectory became horizontal, subjecting the crack tip to the Mode-I condition. Consequently, the F_{11} and F_{22} fields near the crack tip became symmetric about the crack, while F_{12} and F_{21} fields became anti-symmetric about the crack, as expected for Mode-I fracture. The same fields of $F_{\alpha\beta}$, but plotted in the deformed configurations, are shown in Appendix A to illustrate the effect of large deformation and crack blunting. It should be emphasized that the fields of $F_{\alpha\beta}$ were directly measured from the particle tracking data and thus do not depend on any assumptions on the constitutive relation.

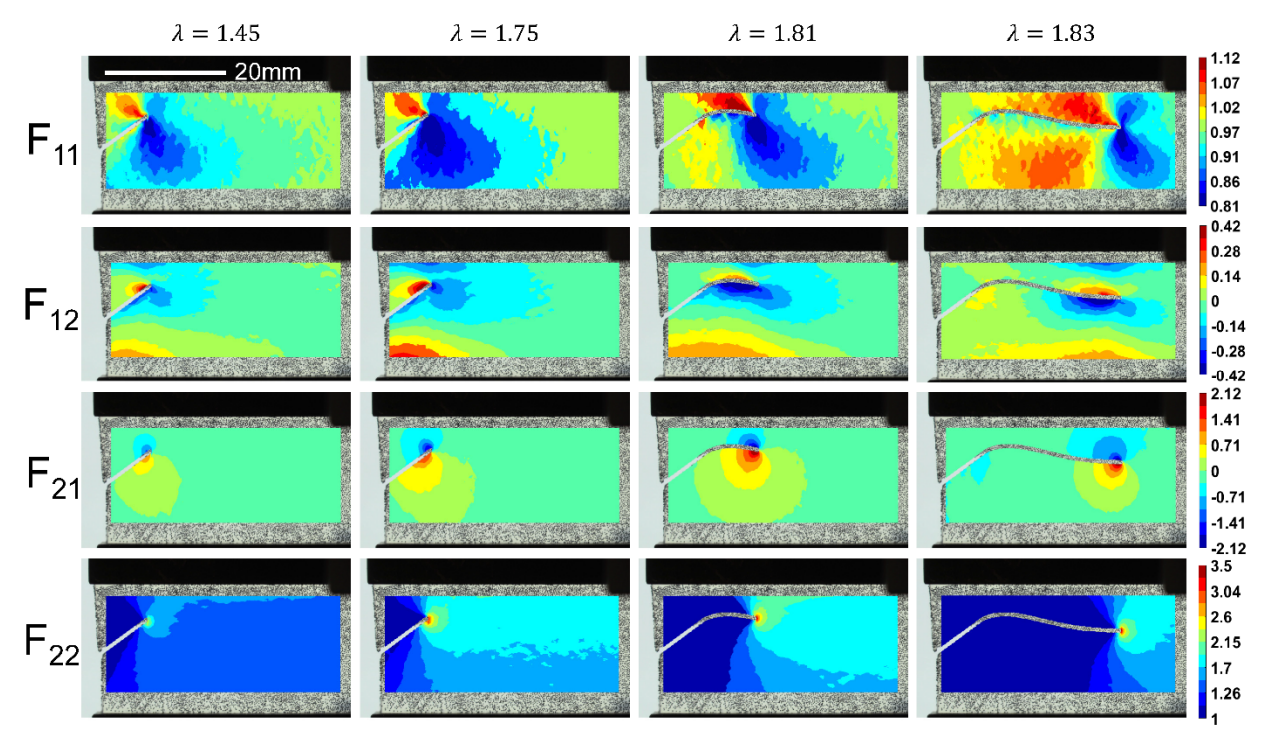


Figure 5 Deformation fields during crack propagation. Color contours of the in-plane deformation gradient components $F_{\alpha\beta}(\alpha, \beta = 1, 2)$ at four frames with different global stretch λ for the case with initial tilt angle $\theta = 30^{\circ}$ are plotted in the reference configuration.

The stress fields were calculated by plugging the experimentally measured F_{ij} into the constitutive model. As mentioned in Section 2, we adopted the incompressible GNH model with the following strain energy density function W:

$$W = \frac{\mu}{2b} \left\{ \left[1 + \frac{b}{n} (I_1 - 3) \right]^n - 1 \right\} , \tag{4}$$

where μ is the shear modulus at infinitesimal strain, I_I is the trace of the left Cauchy-Green tensor $\mathbf{F}\mathbf{F}^T$, and b, n are dimensionless material constants specifying the degree and onset of strain stiffening, respectively. Components of the Cauchy stress tensor $\boldsymbol{\sigma}$ are given by

$$\sigma_{ij} = -p\delta_{ij} + 2\frac{dW}{dI_1}F_{ik}F_{kj}, \ (i, j, k = 1, 2, 3), \tag{5}$$

where p is a Lagrange multiplier enforcing the incompressibility constrain. Note that the summation convention of summing over repeated indices is used throughout this work. We leveraged the plane stress condition that $\sigma_{33} = 0$ to determine p and obtain the following equation for the Cauchy stress components:

$$\sigma_{\alpha\beta} = \mu \left[1 + \frac{b}{n} (I_1 - 3) \right]^{n-1} \left(F_{\alpha\xi} F_{\xi\beta} - \lambda_3^2 \delta_{\alpha\beta} \right) \quad (\alpha, \beta, \xi = 1, 2), \tag{6}$$

where λ_3 is the out-of-plane stretch ratio given in eq. (3). For example, the Cauchy stress fields for the case of initial tilt angle $\theta = 30^{\circ}$ are shown in Fig.6 using the material parameters calibrated from uniaxial tensile tests (see Table 1). Similar to the deformation gradient fields in Fig.5, the stress fields also transitioned from being asymmetric about the initial tilted crack (i.e., the column for $\lambda = 1.45$ and 1.75) to exhibiting a Mode-I structure near the crack tip (i.e., the column for $\lambda = 1.83$).

Because of the nonlinearity associated with large deformation, one can no longer decompose the crack tip deformation and stress fields into the superposition of two separate Mode-I and Mode-II components as in LEFM. To our best knowledge, it is still an open question how to define the mode-mixity under large deformation. Theoretical analyses [15,17] suggested that a measure for mode-mixity may emerge from the leading order asymptotic behavior of the crack tip fields. The full deformation and stress fields obtained in our experiments can provide data to test the theoretical approach for defining mode-mixity. However, such investigations would

require an extensive discussion on the crack tip fields and therefore will be reported in a separate work. The focus of this work is on the fracture toughness and the direction of crack propagation.

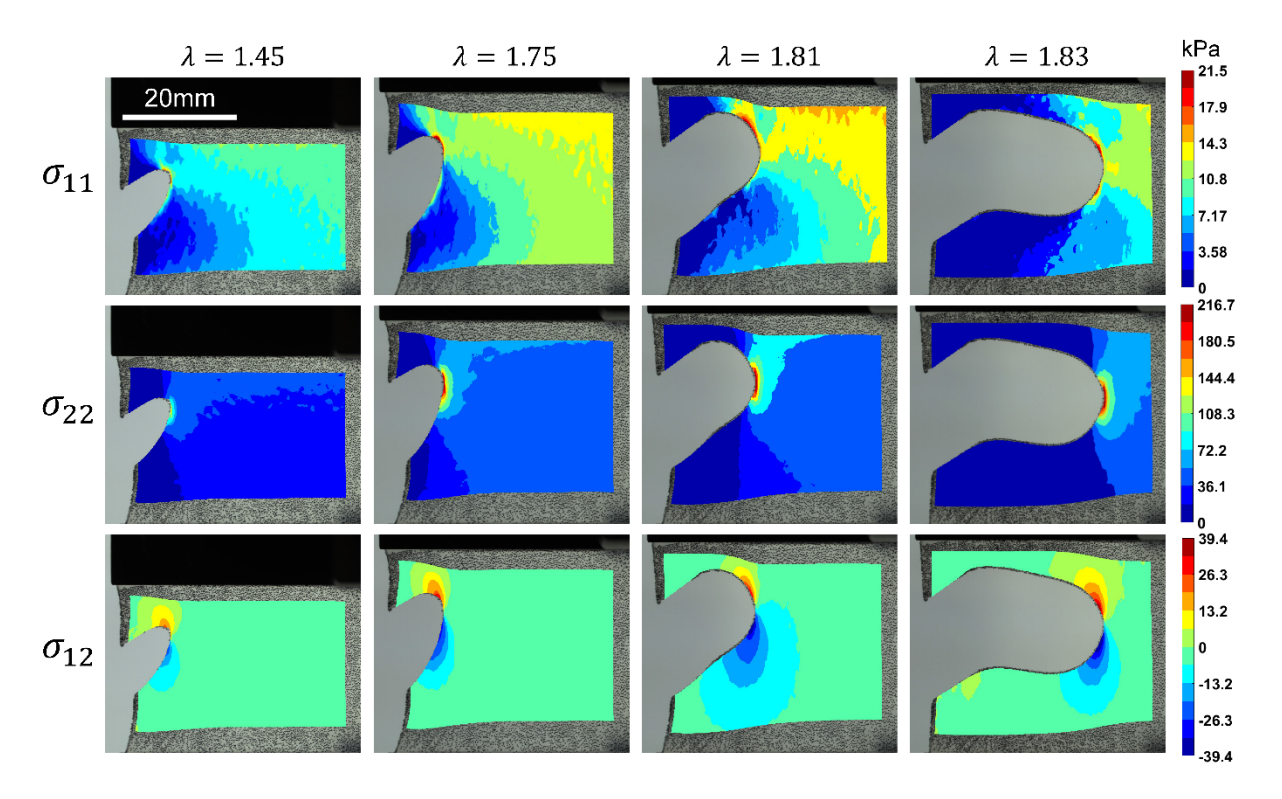


Figure 6 Stress fields during crack propagation. Color contours of Cauchy stress components $\sigma_{\alpha\beta}$ (α , β = 1, 2) at four frames with different global stretch λ for the case with initial tilt angle θ = 30° are plotted in the deformed configurations.

3.3 J-integral

We computed the energy release rate G for each time frame of the fracture test using the J-integral. If the initial orientation and propagation direction of the crack is aligned with the x_1 -axis (e.g., the case of initial tilt angle $\theta = 0^{\circ}$ in Fig.3c), the J-integral is given by [17]:

$$J = \int_{C} \left(W N_{1} - \frac{\partial u_{\alpha}}{\partial x_{1}} S_{\alpha\beta} N_{\beta} \right) ds \qquad (\alpha, \beta = 1, 2),$$
 (7)

where C is a contour in the reference configuration enclosing the crack tip, W is the strain energy density function in eq. (4), N_{β} is the component of the unit outward normal vector of C, $S_{\alpha\beta}$ is the component of the first Piola-Kirchhoff stress tensor S, u_{α} is component of the displacement vector, and s is the arc length along the contour C. The Piola-Kirchhoff stress tensor S is related to the

Cauchy stress tensor σ in eq. (6) by $\mathbf{S} = \det(\mathbf{F})\sigma\mathbf{F}^{-T}$, where $\det(\mathbf{F}) = 1$ due to incompressibility. For the tilted crack in our experiments, the crack propagation took a curved trajectory. Recall that the tangent direction of the reference crack trajectory was identified for each frame, as represented by a local coordinate system $x_1' - x_2'$ (see Fig.4a). Therefore, we recast the J-integral in the local coordinate system $x_1' - x_2'$ as follows, since the x_1' -axis is along the crack propagation direction:

$$J = \int_{C} \left(W N_{1}' - \frac{\partial u_{\alpha}'}{\partial x_{1}'} S_{\alpha\beta}' N_{\beta}' \right) ds, \qquad (8)$$

where u'_{α} , $S'_{\alpha\beta}$, and N'_{β} are components of the displacement **u**, the first Piola-Kirchhoff stress **S**, and the unit normal vector **N** with respect to the $x'_1-x'_2$ coordinate system, respectively. Denote the angle of rotation from the global coordinate system x_1-x_2 to the local coordinate system $x'_1-x'_2$ as ψ (see Fig.7a). Transformation between the global and local coordinates systems can be achieved using the following orthogonal matrix:

$$\begin{bmatrix} Q_{11} & Q_{12} \\ Q_{21} & Q_{22} \end{bmatrix} = \begin{bmatrix} \cos \psi & -\sin \psi \\ \sin \psi & \cos \psi \end{bmatrix}. \tag{9}$$

Specifically, the following equations for transformation:

$$\frac{\partial u'_{\alpha}}{\partial x'_{1}} = Q_{\xi\alpha}Q_{\eta 1}\frac{\partial u_{\xi}}{\partial x_{\eta}}, \ S'_{\alpha\beta} = Q_{\xi\alpha}Q_{\eta\beta}S_{\xi\eta}, \ N'_{\beta} = Q_{\xi\beta}N_{\xi},$$
(10)

where all the indices range from 1 to 2 and the summation convention is used. For the J-integral in eq. (8) to be independent of the contour C and be equal to the energy release rate G, the integrand should be zero on the crack surface. While the second term of the integrand is zero on the crack surface due to the traction-free condition $(S'_{\alpha\beta}N'_{\beta}=0)$, the first term WN'_1 is not necessarily zero because of the curved crack trajectory. To justify eq. (8), we note that W is only non-zero near the crack tip. Since the crack trajectories in all of our experiments only had small curvatures (i.e., no steep change of slope), N'_1 vanishes near the crack tip. Therefore, the integral of WN'_1 along the crack surface should be negligible. We verified this point by evaluating the J-integral along different contours using the measured deformation fields and confirmed that it was indeed path-independent. However, in case of curved cracks with large curvatures, eq. (8) may no longer be valid for evaluating the energy release rate.

We use the case with $\theta=30^\circ$ as an example to demonstrate the calculation of J-integral and show the results in Fig.7a-7c. In this case, the angle ψ of the local coordinate system $x_1'-x_2'$ was first equal to $\theta=30^\circ$ before crack propagation (Fig.7a). After the crack propagation started, ψ first changed from being positive to negative, and then back to nearly zero. In addition, we performed uniaxial tension tests using two strips cut from the unused part of the fracture sample. By fitting the data with the GNH model (Fig.7b), we found that the following parameters: $\mu=20.6$ kPa, b=0.0415, n=2. Using the angle ψ , the measured deformation fields and the material parameters, we evaluated the J-integral in eq. (8) along 9 different paths at each frame (see Fig.7a). The results of J-integral, or the energy release rate G, are plotted in Fig.7c as a function of the global stretch λ , showing that the J-integral calculated based on our measurements was path-independent.

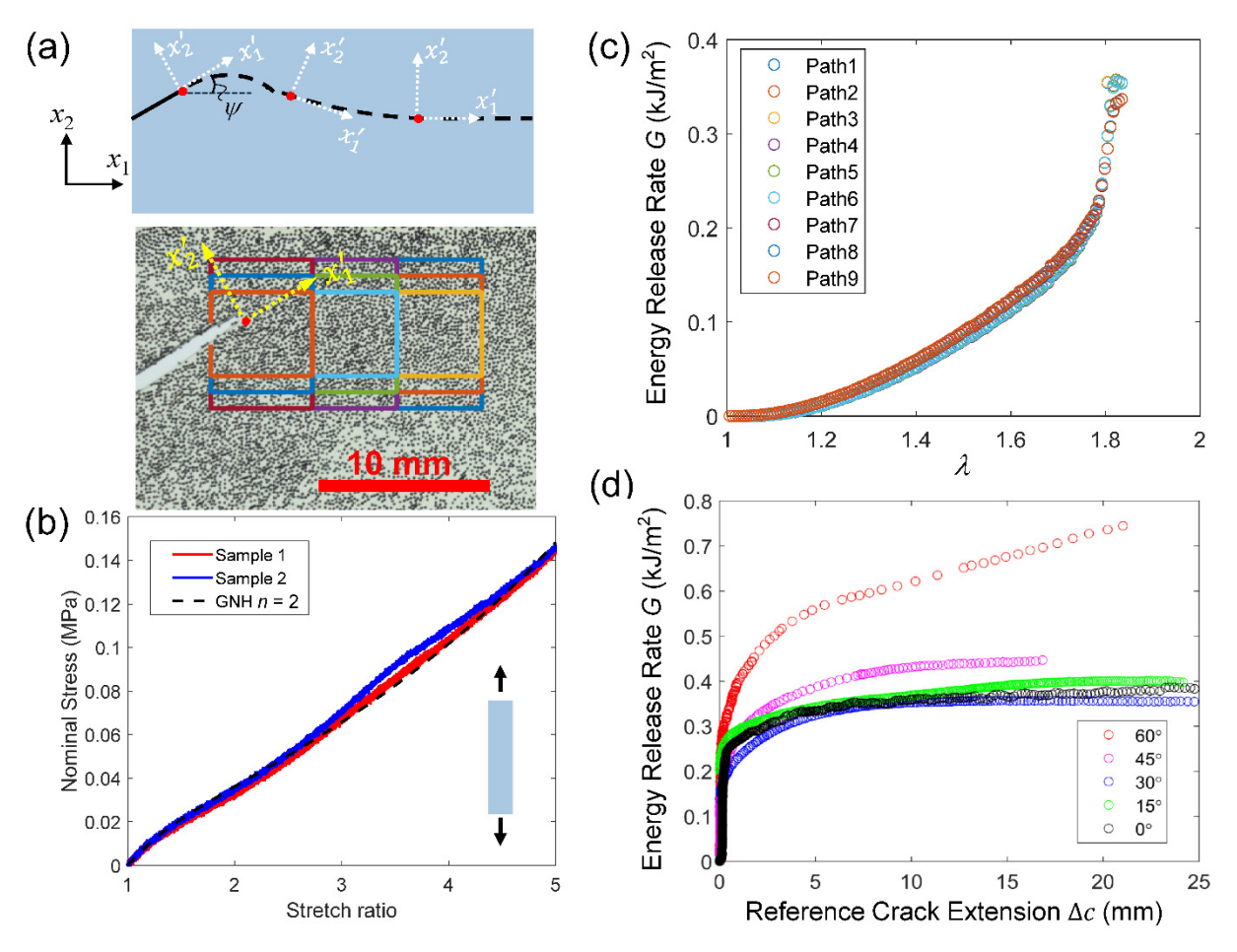


Figure 7 *J-integral and the energy release rate.* (a) Top panel: schematic showing the curved crack trajectory in the reference configuration, the local coordinate system x'_1 - x'_2 and the rotation angle ψ . Bottom panel: 9 paths of *J*-integral used in the case with initial tilt angle $\theta = 30^{\circ}$. (b)

Nominal stress versus stretch ratio of uniaxial tension tests using two strips cut from the sample with initial tilt angle θ = 30°. The dashed line represents the fitting based on the GNH model with μ = 20.6 kPa, b = 0.0415, and n = 2. (c) J-integral calculated using 9 different paths versus global stretch 1 in the case with initial tilt angle θ = 30°. (d) Energy release rate G evaluated using the J-integral versus reference crack extension Δc for five cases with different initial tilt angle θ .

Using the J-integral approach, we measured the energy release rate G during crack propagation for five cases with different initial tilt angles: $\theta = 0^{\circ}$, 15°, 30°, 45°, 60°. With these tilt angles, the initial crack was subjected to different degrees of mode-mixity ranging from pure Mode-I ($\theta = 0^{\circ}$) to strongly mixed mode ($\theta = 60^{\circ}$). For each case, we performed uniaxial tensile tests to calibrate the parameters of the GNH model. It was found that the data for all samples can be well fitted by the GNH model with n = 2, but there were slight variations in μ and b, as listed in Table 1. The average G for 9 different integration paths is plotted in Fig.7d as a function of the reference crack extension Δc for all five cases. We notice that the case of $\theta = 60^{\circ}$ exhibits a more significant increase in G with increasing Δc than the other four cases. This is due to the higher crack speed in the case of $\theta = 60^{\circ}$, which will be elaborated in Section 3.4.

Table 1 Material parameters μ and b of the GNH hyperelastic model (n=2) and the fracture toughness Γ_{in} for the initiation of crack propagation measured for the five cases with different initial crack tilt angle θ .

Initial tilt angle θ (°)	0	15	30	45	60
μ (kPa)	21.4	21.2	20.6	20.4	21.0
b	0.0344	0.042	0.0415	0.0347	0.04
$\Gamma_{in} (kJ/m^2)$	0.154	0.179	0.156	0.167	0.232

3.4 Mixed-mode fracture toughness

The curves in Fig.7d are reminiscent of the crack growth resistance curve, i.e., the R-curve, typically observed in elastic-plastic materials. When the energy release rate G was below a critical value, the crack underwent large deformation but Δc remained zero, indicating that crack propagation had not started yet. After crack propagation started ($\Delta c > 0$), G increased as Δc grew. Given that the crack propagation in our experiments was quasi-static, during crack propagation

G is equal to the fracture toughness Γ . The results in Fig.7d suggest that the elastomer is not characterized by a single value of fracture toughness as in an ideal elastic solid [27].

We define the critical value of G associated with the initiation of crack propagation as the initiation toughness Γ_{in} . The values of Γ_{in} for the five cases with different initial crack tilt angles were extracted from Fig.7d (Table 1 and Fig.8a). Note that uncertainty of the mapping process to locate the crack tip in the reference configuration (see Section 3.1) resulted small noises in Δc . Hence Δc was not exactly zero before crack propagation started. Therefore, we implemented a tolerance threshold for Δc to accommodate potential noises. The Γ_{in} values in Table 1 and Fig.8a were extracted by setting a threshold of 0.15 mm in Δc , which is comparable to the size of the tracer particles. The error bars in Fig.8a were generated by varying the threshold in Δc from 0.1 mm to 0.18 mm. We can see that Γ_{in} was insensitive to the initial tilt angle θ , except that the case of $\theta = 60^{\circ}$ exhibited a slightly higher Γ_{in} than the other cases. Given that there is no consistent trend in the data of Γ_{in} versus θ , we attribute the higher Γ_{in} for $\theta = 60^{\circ}$ to the variation among samples, which may be in terms of the material property or the initial crack (e.g., sharpness of the initial cut). Overall the results in Fig.7a suggest that the fracture toughness corresponding to the onset of crack propagation is independent of the mixed-mode condition.

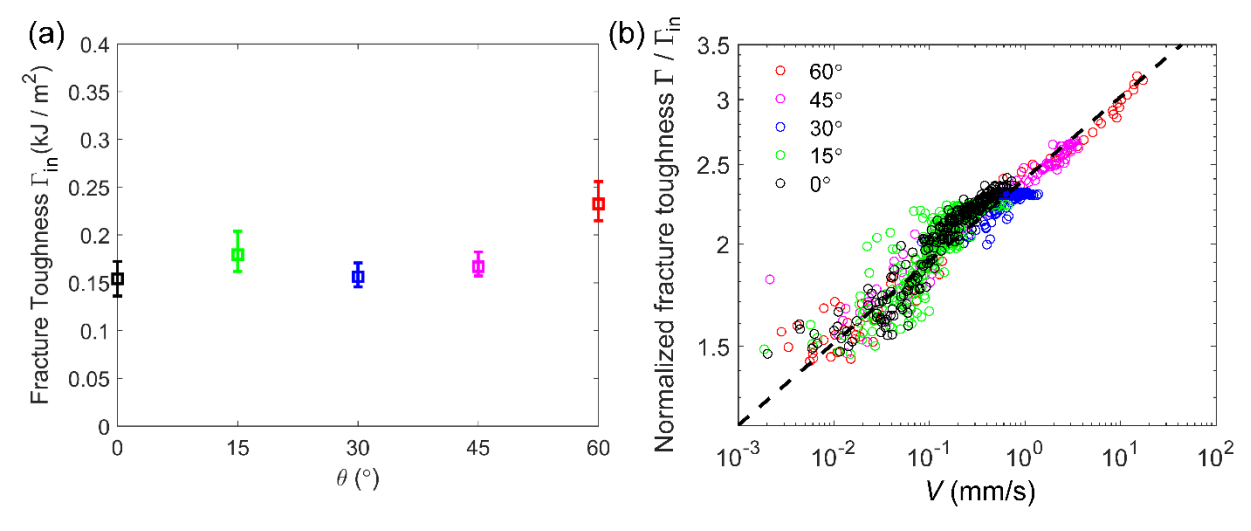


Figure 8 Fracture toughness measured using the tilted cracks. (a) The initiation toughness $\Gamma_{\rm in}$ versus the initial tilt angle θ . The error bars were obtained by varying the tolerance threshold in Δc from 0.1 mm to 0.18 mm when identifying the onset of crack propagation. The symbols were obtained using a threshold of 0.15 mm in Δc . (b) The normalized fracture toughness $\Gamma/\Gamma_{\rm in}$ versus the reference crack speed V for the five cases with different crack tilt angle θ . The dashed line is given by the function $\Gamma/\Gamma_{\rm in} = aV^{0.1}$ with a = 2.4 (mm/s)^{-0.1}.

After the onset of crack propagation, the fracture toughness Γ increased with Δc . More importantly, the measured Γ (i.e., G in Fig.7d) changed as the initial tilt angle θ was increased, especially when $\theta = 60^{\circ}$. To understand this observation, we first note that the R-curves in Fig.7d indicate that the elastomer used in our experiment was not exactly elastic, otherwise the R-curve should be a step function leveled at Γ_{in} . It was reported in our recent work [29] that the Ecoflex 00-30 elastomer under cyclic tensile tests exhibited hysteresis when the stretch ratio was large (> ~ 3), suggesting that bulk energy dissipation may occur in a very small region around the crack tip (size < 0.3mm) [29], similar to the "small scale yielding" condition in LEFM. Such bulk dissipation was responsible for the increase in Γ with crack propagation. Moreover, our previous study [29] on pure Mode-I fracture of the Ecoflex 00-30 elastomer revealed that Γ scaled weakly with the reference crack speed $V: \Gamma \sim V^{0.11}$, indicating that the bulk dissipation was rate-dependent. Motivated by these findings, we hypothesize that the crack growth resistance behavior in Fig.7d, i.e., increasing Γ with Δc , is due to the acceleration of crack propagation after the onset, which is supported by the rapid increase in V found in Fig.4c. Accordingly, the difference in Γ after the onset of crack propagation, as observed in Fig.7d, should be attributed to different crack speeds. For example, the large Γ in the case with $\theta = 60^{\circ}$ was because the crack speed V in this case was much larger than the other cases. To verify this hypothesis, we normalized the Γ after the onset of crack propagation by the initiation toughness Γ_{in} and plotted Γ/Γ_{in} versus the reference crack speed V for all five cases in Fig.8b. The normalization was motivated by the scattering in Γ_{in} (see Fig. 8a). Interestingly, the data points from all five cases with different initial tilt angle θ collapsed to a master curve (Fig.8b), which can be fitted by the following power-law function:

$$\frac{\Gamma}{\Gamma_{in}} = aV^m, \tag{11}$$

with m = 0.1 and a = 2.4 (mm/s)^{-0.1}. The exponent m = 0.1 is close to that found in our previous work [29] (i.e., $\Gamma \sim V^{0.11}$) for pure Mode-I fracture of the same elastomer. Given the variation in the angle ψ (see Fig.7a) during crack propagation, the collapse of data points from all five cases in Fig.8b further demonstrate that the rate-dependence of Γ is also insensitive to the mixed-mode condition.

The data in Fig.8b can also explain the higher R-curve for the case of $\theta=60^\circ$. In the cases with relatively low tilt angles (i.e., $\theta=0^\circ$, 15° and 30°), the crack speed V settled at roughly 1 mm/s (see Fig.8b), which corresponds to the R-curve plateaus in Fig.7d. In contrast, in the case of $\theta=60^\circ$, the crack speed increased rapidly after the initiation of crack propagation and reached 20 mm/s. This rapid increase of crack speed corresponds to the increase in the R-curve for the case of $\theta=60^\circ$. To understand this phenomenon, we note that the energy release rate G depends on both the global loading Δ/H and the crack direction. In the case of $\theta=60^\circ$, when the crack propagation direction transitioned from the initial tilted angle to approximately horizontal (see the bottom row of Fig.3d), the energy release rate G increased substantially, which led to the increase in crack speed. Such effect is not as significant in the cases with lower tilt angles, since the change in the crack propagation direction was not as large.

Recall that in Fig.3 we observed severe blunting of the crack tip due to the large crack opening displacement. The extent of crack opening can be estimated using the nonlinear length scale Γ/E , where E is the Young's modulus of the elastomer [33]. This length scale describes the crack opening displacement as well as the size of the crack tip nonlinear zone during crack propagation [34]. Assuming incompressibility for the elastomer, we have $E = 3\mu \approx 60$ kPa (see Table 1). Using the values of initiation toughness in Fig.8a, i.e., Γ_{in} ranging from 154 to 232 J/m², we find that $\Gamma_{\rm in}/E$ is 2.6 to 3.9 mm. After the crack started to propagate, the fracture toughness Γ is larger and can reach 350 to 700 J/m² (see Fig.7d), which implies $\Gamma/E = 5.8$ to 12.5 mm. The nonlinear length scale, in terms of either Γ_{in}/E or Γ/E , is comparable to the sample height (H = 22 mm), indicating significant nonlinear effects in our crack propagation experiments. However, it should be emphasized that crack blunting does not affect our data analysis. Although the crack tip is blunted in the deformed configuration, it is sharp when mapped back to the reference configuration (e.g., see Fig.4). This is consistent with our approach of evaluating the J-integral in the reference configuration to determine the energy release rate. On the other hand, crack blunting may affect the fracture process at the crack tip. Even for the tilted cracks, after crack blunting the crack tip deformation field was still dominated by the F_{22} component (see Fig. 5 and Fig. 10). Based on this observation, we speculate that the crack tip process zone is primarily subjected to tensile loading, despite the global mixed-mode condition introduced by the tilted crack, which may explain why the fracture toughness is mode-independent.

3.5 Direction of crack propagation

Finally, we examine the direction of crack propagation, which was identified as the tangent of the crack trajectory in the reference configuration. As mentioned in Section 3.1, in all cases with different initial tilt angle θ , the crack trajectory eventually became horizontal, i.e., perpendicular to the global tensile loading. This observation leads us to hypothesize that the crack propagation direction is perpendicular to the direction of maximum principal stretch ahead of the crack tip. Both of these directions should be with respect to the reference configuration. Specifically, the crack propagation direction is represented by the local x_1' -axis (Figs.9a), while the direction of maximum principal stretch can be determined by solving the eigenvectors of the right Cauchy-Green tensor, $\mathbf{C} \equiv \mathbf{F}^T \mathbf{F}$. It is worth pointing out that for isotropic hyperelastic solids, the principal directions of \mathbf{C} are aligned with those of the second Piola-Kirchhoff stress tensor. Therefore, the maximum principal stretch direction is also the maximum principal direction of the second Piola-Kirchhoff stress.

We verify the hypothesis stated above by computing the direction of maximum principal stretch at the crack tip using the deformation fields measured. To mitigate the uncertainties of particle tracking and MLS interpolation, instead of directly evaluating C at the crack tip, for each frame we constructed a 5×5 square grid in the reference configuration, with the center grid point in the first column located at the crack tip and the spacing between adjacent grid points being 0.1 mm (see inset of Fig.9a for example). We then computed the tensor C and its maximum principal direction at each grid point, and took the average vector over the 25 grid points as the direction of maximum principal stretch, as illustrated by the blue arrows in Fig.9a. The angle between the local x_1' -axis and the direction of maximum principal stretch, denoted as $\gamma (\geq 0)$, was used to quantify the relative orientation of these two directions. Figure 9b plots the value of γ versus the reference crack extension length Δc for all five cases. The inset shows an example of the reference crack trajectory and the directions of maximum principal stretch every five frames. Despite the noises, it can be seen that γ remained close to 90°, which verifies our hypothesis. This result suggests that one may use the direction of maximum principal stretch directly ahead of the crack tip to predict the crack propagation direction in the Ecoflex 00-30 or similar elastomers, which can facilitate computational modeling of mixed-mode crack propagation with curved trajectory.

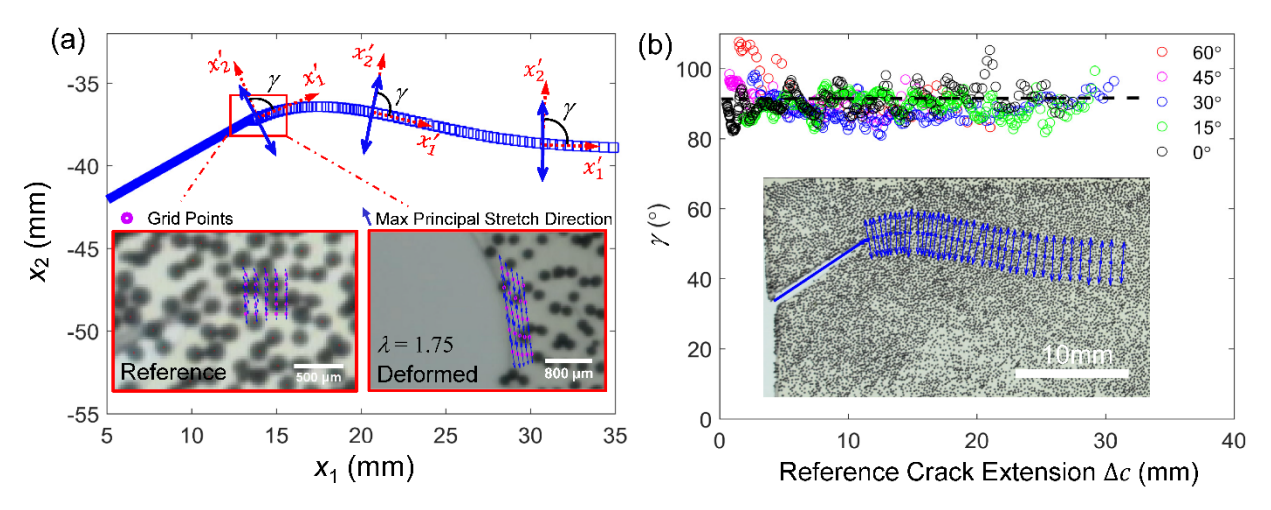


Figure 9 Direction of crack propagation. (a) Crack trajectory in the case with initial tilt angle $\theta = 30^{\circ}$. The local coordinate system x'_1 - x'_2 , the direction of maximum principal stretch (blue arrows) and the angle γ are schematically shown. The left inset shows the 5×5 square grid in the reference configuration with the maximum principal stretch direction on each grid point when the global stretch λ is 1.75. The right inset shows the corresponding grid points and maximum principal stretch directions (i.e., eigenvector of the left Cauchy-Green tensor $\mathbf{B} = \mathbf{F}\mathbf{F}^{\mathrm{T}}$) in the deformed configuration. (b) The angle γ versus reference crack extension Δc for the five cases with different initial tilt angle θ . The inset shows an example of the reference crack trajectory and the maximum principal stretch directions (every five frames) using the case with $\theta = 30^{\circ}$ as an example.

4. Conclusion

We presented an experimental study on the mixed-mode crack propagation (i.e., Mode I and II) in thin-sheet samples of a soft silicone elastomer. The mixed-mode condition was achieved by introducing an inclined crack at the edge of the pure shear fracture sample. The degree of mode-mixity was controlled by varying the initial tilt angle of the crack. We observed that the tilted crack followed a curved trajectory once it started to propagate. Using the particle tracking method, we were able to measure the displacement and deformation gradient fields at any frame during our experiments. These fields enabled us to monitor the trajectory of crack tip in the reference configuration and further determine the reference crack extension length Δc , the reference crack speed V and the direction of crack propagation. More importantly, by combining the measured deformation gradient fields and the calibrated GNH hypereleatic model for the elastomer, we determined the energy release rate G using the J-integral approach, based on which we measured the fracture toughness for cracks with different initial tilt angles.

Our data revealed that both the initiation toughness Γ_{in} , which corresponds to the onset of crack propagation, and the subsequent rate-dependent toughness, as manifested in the function Γ/Γ_{in} versus reference crack speed V, were insensitive to the initial tilt angle θ . This finding suggests that the elastomer used in our experiments exhibits mode-independent fracture toughness, at least within the range of mode-mixity attained in our experiments. Regarding the direction of crack propagation (i.e., the tangent direction of crack trajectory in the reference configuration), we found that it was approximately perpendicular to the direction of maximum principal stretch ahead of the crack tip in the reference configuration. These experimental results can provide insights towards establishing criteria for modeling curved crack propagation under mixed-mode loading. More broadly, the test configuration with tilted crack and the particle tracking method can be extended to any predominantly elastic elastomer or gels, therefore opening a new paradigm for measuring the mixed-mode fracture toughness of soft materials.

Acknowledgement

The authors acknowledge funding support from National Science Foundation through a CAREER award (NSF CMMI-1752449).

Appendix A Deformation gradient fields in the deformation configurations

Figure 10 below shows the fields of deformation gradient components $F_{\alpha\beta}$ (α , $\beta = 1, 2$) corresponding to those in Fig.5 but plotted in the deformed configurations.

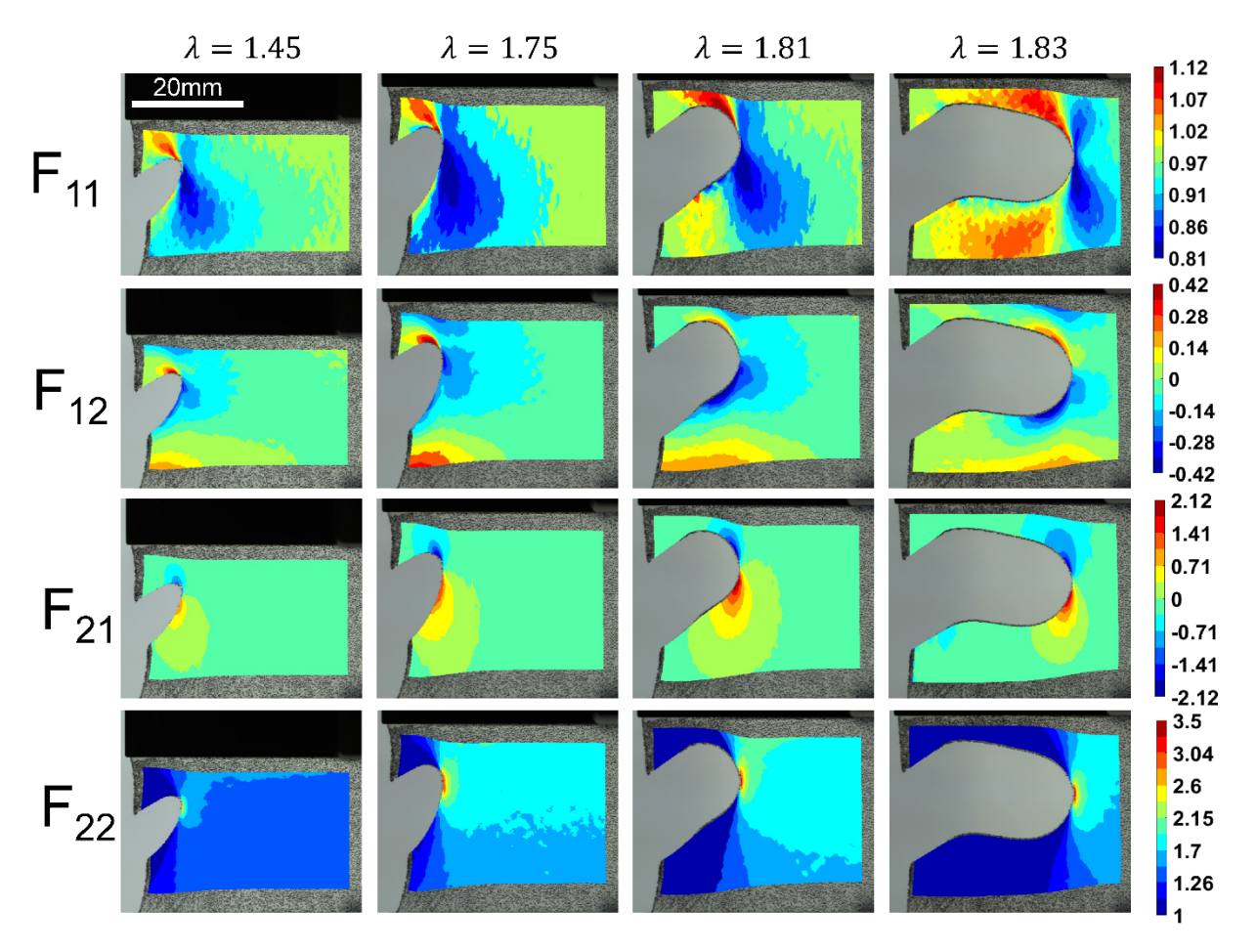


Figure 10 Deformation fields during crack propagation. Color contours of the in-plane deformation gradient components $F_{\alpha\beta}(\alpha, \beta = 1, 2)$ at four frames with different global stretch λ for the case of initial tilt angle $\theta = 30^{\circ}$ are plotted in the deformed configurations.

Reference

- [1] L. Dong, H. Jiang, Autonomous microfluidics with stimuli-responsive hydrogels, Soft Matter. 3 (2007) 1223–1230. https://doi.org/10.1039/b706563a.
- [2] C. Creton, Pressure-sensitive adhesives: An introductory course, MRS Bull. 28 (2003) 434–439. https://doi.org/10.1557/mrs2003.124.

- [3] H. Yuk, S. Lin, C. Ma, M. Takaffoli, N.X. Fang, X. Zhao, Hydraulic hydrogel actuators and robots optically and sonically camouflaged in water, Nat. Commun. 8 (2017) 14230. https://doi.org/10.1038/ncomms14230.
- [4] K. Yasuda, J.P. Gong, Y. Katsuyama, A. Nakayama, Y. Tanabe, E. Kondo, M. Ueno, Y. Osada, Biomechanical properties of high-toughness double network hydrogels, Biomaterials. 26 (2005) 4468–4475. https://doi.org/10.1016/j.biomaterials.2004.11.021.
- [5] C. Keplinger, J.-Y. Sun, C.C. Foo, P. Rothemund, G.M. Whitesides, Z. Suo, Stretchable, Transparent, Ionic Conductors, Science (80-.). 341 (2013) 984–987. https://doi.org/10.1126/science.1240228.
- [6] R.S. Rivlin, A.G. Thomas, Rupture of rubber. I. Characteristic energy for tearing, J. Polym. Sci. 10 (1953) 291–318. https://doi.org/10.1002/pol.1953.120100303.
- [7] J.P. Gong, Why are double network hydrogels so tough?, Soft Matter. 6 (2010) 2583–2590. https://doi.org/10.1039/b924290b.
- [8] C. Creton, M. Ciccotti, Fracture and adhesion of soft materials: a review, Reports Prog. Phys. 79 (2016). https://doi.org/10.1088/0034-4885/79/4/046601.
- [9] X. Zhao, Multi-scale multi-mechanism design of tough hydrogels: Building dissipation into stretchy networks, Soft Matter. 10 (2014) 672–687. https://doi.org/10.1039/c3sm52272e.
- [10] R. Bai, J. Yang, Z. Suo, Fatigue of hydrogels, Eur. J. Mech. A/Solids. 74 (2019) 337–370. https://doi.org/10.1016/j.euromechsol.2018.12.001.
- [11] H.W. Greensmith, Rupture of rubber. X. The change in stored energy on making a small cut in a test piece held in simple extension, J. Appl. Polym. Sci. 7 (1963) 993–1002. https://doi.org/10.1002/app.1963.070070316.
- [12] A.N. Gent, Adhesion and strength of viscoelastic solids. Is there a relationship between adhesion and bulk properties?, Langmuir. 12 (1996) 4492–4495. https://doi.org/10.1021/la950887q.
- [13] X. Ni, C. Chen, J. Li, Interfacial fatigue fracture of tissue adhesive hydrogels, Extrem. Mech. Lett. 34 (2020) 100601. https://doi.org/10.1016/j.eml.2019.100601.

- [14] J. Yang, R. Bai, B. Chen, Z. Suo, Hydrogel Adhesion: A Supramolecular Synergy of Chemistry, Topology, and Mechanics, Adv. Funct. Mater. 30 (2020) 1901693. https://doi.org/10.1002/adfm.201901693.
- [15] R.A. Stephenson, The equilibrium field near the tip of a crack for finite plane strain of incompressible elastic materials, J. Elast. 12 (1982) 65–99. https://doi.org/10.1007/BF00043706.
- [16] K.C. Le, H. Stumpf, The singular elastostatic field due to a crack in rubberlike materials, J. Elast. 32 (1993) 183–222. https://doi.org/10.1007/BF00131660.
- [17] P.H. Geubelle, W.G. Knauss, Finite strains at the tip of a crack in a sheet of hyperelastic material: I. Homogeneous case, J. Elast. 35 (1994) 61–98. https://doi.org/10.1007/BF00115539.
- [18] J.K. Knowles, A nonlinear effect in mode II crack problems, Eng. Fract. Mech. 15 (1981) 469–476. https://doi.org/10.1016/0013-7944(81)90072-2.
- [19] R. Harpaz, E. Bouchbinder, A nonlinear symmetry breaking effect in shear cracks, J. Mech. Phys. Solids. 60 (2012) 1703–1709. https://doi.org/10.1016/j.jmps.2012.06.010.
- [20] Z. Wang, C. Xiang, X. Yao, P. Le Floch, J. Mendez, Z. Suo, Stretchable materials of high toughness and low hysteresis, Proc. Natl. Acad. Sci. U. S. A. 116 (2019) 5967–5972. https://doi.org/10.1073/pnas.1821420116.
- [21] C. Li, H. Yang, Z. Suo, J. Tang, Fatigue-Resistant elastomers, J. Mech. Phys. Solids. 134 (2020) 103751. https://doi.org/10.1016/j.jmps.2019.103751.
- [22] L.M. Cox, A.K. Blevins, J.A. Drisko, Y. Qi, Y. Ding, C.I. Fiedler-Higgins, R. Long, C.N. Bowman, J.P. Killgore, Tunable Mechanical Anisotropy, Crack Guiding, and Toughness Enhancement in Two-Stage Reactive Polymer Networks, Adv. Eng. Mater. 21 (2019) 1900578. https://doi.org/10.1002/adem.201900578.
- [23] G.P. Anderson, K.L. DeVries, M.L. Williams, The peel test in experimental adhesive-fracture mechanics Paper demonstrates the potential use of peel tests in obtaining adhesive-fracture-energy values, Exp. Mech. 16 (1976) 11–15. https://doi.org/10.1007/BF02328915.

- [24] T.L. Sun, T. Kurokawa, S. Kuroda, A. Bin Ihsan, T. Akasaki, K. Sato, M.A. Haque, T. Nakajima, J.P. Gong, Physical hydrogels composed of polyampholytes demonstrate high toughness and viscoelasticity, Nat. Mater. 12 (2013) 932–937. https://doi.org/10.1038/nmat3713.
- [25] O. Ronsin, C. Caroli, T. Baumberger, Crack front échelon instability in mixed mode fracture of a strongly nonlinear elastic solid, EPL. 105 (2014) 34001. https://doi.org/10.1209/0295-5075/105/34001.
- [26] A.T. Zehnder, Fracture Mechanics, Springer Verlag, 2012. https://doi.org/10.1007/978-94-007-2595-9_6.
- [27] R. Long, C.Y. Hui, Fracture toughness of hydrogels: Measurement and interpretation, Soft Matter. 12 (2016) 8069–8086. https://doi.org/10.1039/c6sm01694d.
- [28] J.R. Rice, A path independent integral and the approximate analysis of strain concentration by notches and cracks, J. Appl. Mech. Trans. ASME. 35 (1968) 379–386. https://doi.org/10.1115/1.3601206.
- [29] Y. Qi, Z. Zou, J. Xiao, R. Long, Mapping the nonlinear crack tip deformation field in soft elastomer with a particle tracking method, J. Mech. Phys. Solids. 125 (2019) 326–346. https://doi.org/10.1016/j.jmps.2018.12.018.
- [30] X. Feng, M.S. Hall, M. Wu, C.Y. Hui, An adaptive algorithm for tracking 3D bead displacements: Application in biological experiments, Meas. Sci. Technol. 25 (2014) 55701. https://doi.org/10.1088/0957-0233/25/5/055701.
- [31] W. Liu, R. Long, Constructing Continuous Strain and Stress Fields From Spatially Discrete Displacement Data in Soft Materials, J. Appl. Mech. 83 (2015) 011006. https://doi.org/10.1115/1.4031763.
- [32] T. Belytschko, Y.Y. Lu, L. Gu, Element-free Galerkin methods, Int. J. Numer. Methods Eng. 37 (1994) 229–256. https://doi.org/10.1002/nme.1620370205.
- [33] C. Creton, M. Ciccotti, Fracture and adhesion of soft materials: a review, Reports Prog. Phys. 79 (2016) 046601. https://doi.org/10.1088/0034-4885/79/4/046601.
- [34] R. Long, C.Y. Hui, J.P. Gong, E. Bouchbinder, The Fracture of Highly Deformable Soft

Materials: A Tale of Two Length Scales, Annu. Rev. Condens. Matter Phys. 12 (2021) 71–94. https://doi.org/10.1146/annurev-conmatphys-042020-023937.